Effects of shear-thinning fluids on residual oil formation in microfluidic pore networks

Antonio Rodríguez de Castro [a], Mart Oostrom [b], Nima Shokri [a,*]

[a] School of Chemical Engineering and Analytical Science, The University of Manchester, Manchester M13 9PL, United Kingdom
[b] Energy & Environment Division, Pacific Northwest National Laboratory, Richland, WA, USA

GRAPHICAL ABSTRACT

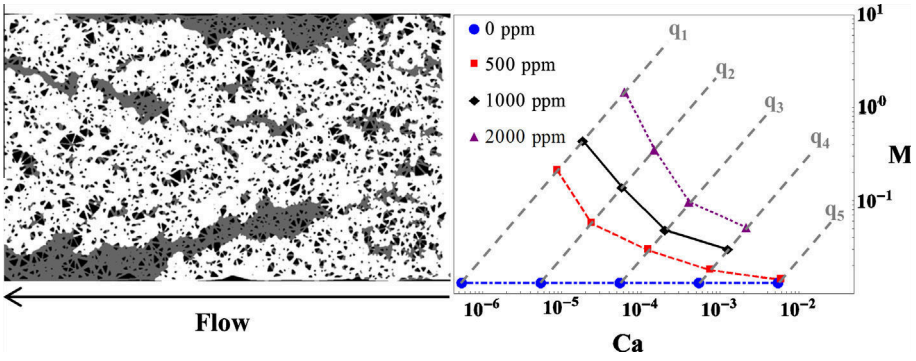

Keywords:
Shear-thinning fluids
Microfluidic analysis
Polymer flooding
Oil recovery
Immiscible displacement

ABSTRACT

Two-phase immiscible displacement in porous media is controlled by capillary and viscous forces when gravitational effects are negligible. The relative importance of these forces is quantified through the dimensionless capillary number Ca and the viscosity ratio M between fluid phases. When the displacing fluid is Newtonian, the effects of Ca and M on the displacement patterns can be evaluated independently. However, when the injecting fluids exhibit shear-thinning viscosity behaviour the values of M and Ca are interdependent. Under these conditions, the effects on phase entrapment and the general displacement dynamics cannot be dissociated. In the particular case of shear-thinning aqueous polymer solutions, the degree of interdependence between M and Ca is determined by the polymer concentration. In this work, two-phase immiscible displacement experiments were performed in micromodels, using shear-thinning aqueous polymer solutions as displacing fluids, to investigate the effect of polymer concentration on the relationship between Ca and M, the recovery efficiency, and the size distribution of the trapped non-wetting fluid. Our results show that the differences in terms of magnitude and distribution of the trapped phase are related to the polymer concentration which influences the values of Ca and M.

1. Introduction

On average, two-thirds of the original oil in geological reservoirs remains unrecovered, even after waterflooding [1,2]. The unrecovered oil becomes trapped in the reservoir forming discontinuous or continuous phase in swept or unswept reservoirs zones,

* Corresponding author at: School of Chemical Engineering and Analytical Science, Room C26, The Mill, The University of Manchester, Sackville Street, Manchester M13 9PL, United Kingdom.
E-mail address: nima.shokri@manchester.ac.uk (N. Shokri).

http://dx.doi.org/10.1016/j.jcis.2016.03.027

respectively [1,3]. Reducing the amount of trapped oil is economically very important and is a subject of ongoing research. The amount of trapped oil and the size of the trapped blobs depend on a variety of parameters including (but not limited to) transport properties of porous media and the physical and chemical properties of the displacing and displaced fluid [4–9].

When gravitational forces are negligible, the two-phase immiscible displacement at the pore level is controlled by the competition between capillary and viscous forces whose relative importance is quantified through two dimensionless numbers: the capillary number Ca and the viscosity ratio M. Ca is often defined as:

$$Ca = \frac{q\mu_1}{\sigma} \quad (1)$$

where q is the Darcy velocity, μ_1 the viscosity of the displacing fluid, and σ the interfacial tension between displacing and resident phases [10,11]. The Darcy velocity q is obtained by dividing the flow rate of the invading fluid (Q) by the cross-sectional area of the porous medium (A). The viscosity ratio M is defined as:

$$M = \frac{\mu_1}{\mu_2} \quad (2)$$

where μ_2 is the viscosity of the resident fluid. The displacement is considered to be favourable if $M > 1$ and unfavourable if $M < 1$. Depending on the values of Ca and M, capillary fingering, viscous fingering, or stable displacement may be observed, influencing flow patterns and phase entrapment during immiscible two-phase flow in porous media [12–16].

The effect of M and Ca on the residual oil saturation at macroscale has been extensively discussed in literature [12,17]. At small Ca, when viscous forces are negligible and capillary fingering prevails, the patterns described by the invading fluid during imbibition will follow the percolation pathways without any specific direction compared to the flow direction [13]. These patterns are described through the invasion percolation statistical approach [18]. On the other hand, viscous fingering is often modelled through diffusion-limited aggregation [19] and gives rise to tree-like fingers oriented in the direction of flow [13]. Viscous fingers are common features of unstable displacements in which water is more mobile than oil [20]. Since Ca has a significant impact on the amount of trapped fluid, often the residual saturation S_{ro} is experimentally measured as a function of Ca to obtain the so-called Capillary Desaturation Curve (CDC) [14], with S_{ro} (Ca) = (volume of the residual oil at the given Ca)/(total pore volume). The CDC is one of the most important input parameters in the reservoir simulation software for enhanced oil recovery [9,21].

Some of the most popular injecting fluids used in Enhanced Oil Recovery (EOR) and in soil remediation practices are non-Newtonian such as polymer solutions, foams or emulsions, and present shear-thinning behaviour, i.e. the viscosity of the fluid decreases as the applied shear stress increases. One of the main purposes of applying these complex fluids is to reduce mobility ratio [22]. This results in viscous fingering reduction and therefore improved sweep efficiency in the reservoir [23]. When a shear-thinning fluid is used as a displacing fluid, both Ca and M are functions of Q (note that μ_1 used in the definition of Ca and M stands for the apparent viscosity of the displacing fluid in the porous medium at a given flow rate). As a consequence, an evaluation of the effects of Ca on S_{ro} and trapped blob sizes assuming a constant M is not acceptable for most shear-thinning fluid displacements.

Several groups investigated the non-Newtonian fluid flow in porous media and its potential application for oil displacement [24–26]. For example, flooding experiments using shear-thinning polymer solutions were previously conducted [20,27] in order to analyse the effect of polymer concentration on front stabilisation and recovery efficiency at a unique flow rate. Other authors [28] carried out computational fluid dynamics simulations using a digitalised pore network to investigate the non-Newtonian fluid displacement at the microscale and compared their results with the flooding experiments [20]. In previous work [2], a micromodel study was performed to investigate the effects of rheological properties of several complex fluids used in EOR on oil recovery.

In subsurface remediation, shear-thinning fluids have been used to create hydraulic stable zones [29] and to force chemical amendments into low permeability zones [30–33]. Although most remediation studies using shear-thinning fluids consist of laboratory experiments, a recent field implementation was reported [34]. Emplacement of amendments into low permeability zones is of particular interest because contaminants in such zones might sustain persistent plumes in adjacent transmissive zones due to diffusion-controlled release processes [35]. Injection of a shear-thinning fluid into a heterogeneous subsurface induces cross-flow between higher- and lower-permeability layers. Mobility reduction behind the polymer solution in a higher-permeability layer then creates a transverse pressure gradient that promotes fluid migration into less permeable layers [32]. In most remediation studies, the shear-thinning fluid contained the biopolymer xanthan [33,34].

Motivated by the widespread use of shear-thinning fluids in porous media and its great potentials in enhanced oil recovery and soil remediation, the specific objectives of the present study are to investigate how Ca and M affect S_{ro} and trapped blob distributions during immiscible two-phase flow in porous media involving shear-thinning fluids. To do so, a comprehensive series of polymer waterflooding displacement experiments were conducted using micromodels with well-defined characteristics to quantitatively investigate the effects of the polymer concentration C_p on oil entrapment patterns, visualised by means of a high resolution microscope at different flow rates. The findings of this paper extend our understanding of the physics governing two-phase flow in porous media using shear-thinning fluids.

2. Materials and methods

2.1. Micromodel

A series of experiments was conducted displacing resident silicone fluid by aqueous polymer solutions in a micromodel. The micromodel was fabricated in a silicon wafer using standard photolithography and inductively coupled plasma–deep reactive ion etching (ICP-DRIE) methods. Details of the fabrication process can be found elsewhere [36]. After the incorporation of nanoports serving as the inlet and outlet of the micromodel, the micromodel was chemically treated to be cleaned and to acquire uniform wettability. After the cleaning procedure, micromodels have a uniform and stable hydrophilic behaviour with contact angles < 16° [37]. The pore-network compartment of the micromodel has a length of 1.4 cm, a width of 0.7 cm, and a thickness of 29 ± 1 μm. The flow network had approximately 3000 pore bodies and 9000 pore throats, resulting in a porosity ε of 0.6. The topology of flow network was based on truncated log-normal for the pore-body distribution and is considered to be a good approximation for pore size distribution in natural porous media [38]. The size of the pore throats was assigned by employing a concept previously proposed in the literature [7], where the size of a pore throat is a function of the dimensions of the connecting pore bodies. The width of the pore bodies varied from 80 to 160 μm, while the width of the pore throats varied from 56 to 159 μm. The pore bodies are cylinders and the pore throats are parallelepipeds. In planar view, pore bodies are circular while pore throats are rectangular, with a minor

deviation from this arrangement due to overlapping. The pore and throat size distribution of the micromodel together with the patterns of channels' distribution have been recently presented [9] thus it is not repeated here. The permeability of the micromodel k, determined by injecting water with different flow rates and measuring the pressure drop, was 2.87×10^{-12} m^2.

2.2. Fluid properties

The used resident fluid was Xiameter® PMX – 200 Silicone Fluid (Dow Corning, UK) with a dynamic viscosity of 1×10^{-1} Pa s (provided by Dow Corning), and an oil–water interfacial tension of 31 ± 1 mN/m, measured by a digital tensiometer (Krüss, K11MK4). The displacing fluids were aqueous solutions with dissolved xanthan gum powder concentrations of 0, 500, 1000, and 2000 ppm. The solutions were prepared by dissolving xanthan in de-ionized and filtered water containing 400 ppm of NaN_3 as a bactericide. Xanthan gum is a commonly used viscosifier [39,40] especially in manufacturing food grade products [41], and is obtained through fermentation of Xanthomonas campestris bacteria [39,41,42]. Additional information about its chemical composition, structure and other physico-chemical properties can be found elsewhere [43]. Its semi dilute xanthan solutions are known to develop a high viscosity level at low shear rates $\dot{\gamma}$ before displaying a drastic decrease when the applied shear rate is increased, and are commonly classified as shear-thinning fluids. In the solution state, an isolated xanthan macromolecule is more or less rigid, its contour length is of typically 1 μm [44], and its transverse size is approximately 2 nm. No plugging effect is expected in the case of micromodels, whose pores are typically larger than 1 μm. Under high flow velocities the shear rate may be such that the xanthan molecules are oriented in the direction of the flow, resulting in a decrease in viscosity.

Addition of polymer did not significantly alter the interfacial tension within the range of concentrations C_p used in this study. The polymer solutions were characterized by means of a stress controlled rheometer (ARG2, TA Instruments) equipped with a cone-plate geometry, following a procedure previously presented in the literature [45,46]. Each shear rate corresponding to a specific shear stress was recorded when its variation was less than a prescribed tolerance (typically 3%) within a given time period. The obtained rheograms are displayed on Fig. 1(a) and the effective viscosities as a function of shear rate are shown in Fig. 1(b). The range of C_p and the measured rheograms in our experiments are similar to those presented by other authors [20], who used aqueous associative polymer solutions in their micromodel displacement experiments.

In the case of semi dilute aqueous xanthan polymer solutions, shear-thinning behaviour is often represented through the empirical Carreau model [47]. The Carreau equation is based on molecular network theory and is often presented as:

$$\frac{\mu - \mu_\infty}{\mu_0 - \mu_\infty} = \left[1 + (\lambda\dot{\gamma})^2\right]^{\frac{n-1}{2}} \quad (3)$$

where μ is the viscosity at a given shear rate $\dot{\gamma}$, μ_0 and μ_∞ are the zero shear rate and infinite shear rate viscosities, respectively, n is the power-law index, and λ is the time constant. The values of μ_0, μ_∞, n and λ are determined by the polymer concentration under given pressure and temperature conditions. The Carreau model was fitted to the data shown in Fig. 1(b) by obtaining the values for μ_0, μ_∞, n, λ, and δ that minimise the sum $\sum_i[\tilde{\tau}_i - \mu(\dot{\gamma}_i)\dot{\gamma}_i]^2\dot{\gamma}_i^\delta$ for each xanthan concentration [45]. In the expression for the sum, $\mu(\dot{\gamma})$ is the Carreau viscosity according to Eq. (3) and $\dot{\gamma}_i$ and $\tilde{\tau}_i$ are the steady state experimental shear stresses and the corresponding shear rates obtained by the rheometer, respectively. The corresponding values of Carreau parameters and δ are presented in Table 1. The relations in Fig. 1(b) show that higher C_p values result in higher viscosities and that the measured data are well described by the Carreau model [47]. The data in Table 2 illustrate that the Newtonian viscosities of xanthan gum solutions increase with increasing C_p, while the onset of shear-thinning behaviour (1/λ) decreases. Besides, the value of n decreases with increasing C_p, reflecting that the shear-thinning behaviour is more pronounced at higher C_p.

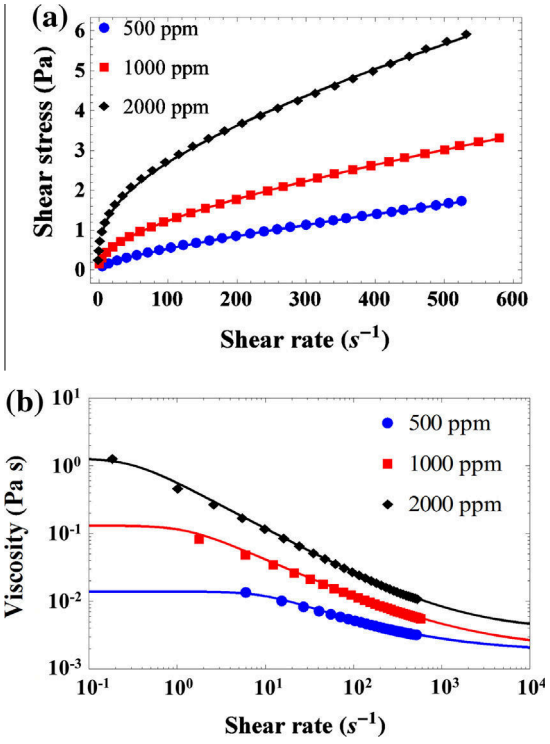

Fig. 1. (a) Rheograms and (b) effective viscosity vs. shear rate for the polymer concentrations of the injected fluid. The symbols represent experimental data and solid lines represent the fitted curves using the Carreau model (Eq. (3)).

2.3. Displacement experiments

The experiments consisted of displacement of resident silicone fluid by four aqueous polymer solutions (0, 500, 1000, and 2000 ppm xanthan), at five flow rates. An overview of the displacement flow rates and associated Darcy velocities are presented in Table 2. The listed experiments were conducted for all four concentrations and were repeated five times. For each concentration, a total of 25 experiments (five repetitions for each of the five flow rates) were completed. The 25 experiments for a given concentration were considered to be an experimental set. The oil – water (0 ppm xanthan) fluid pair was considered to be a reference for comparison between waterflooding and polymer waterflooding using the 500, 1000, and 2000 ppm xanthan solutions. Single stage polymer waterflooding was used in this study. Other authors [2] showed that a single stage recovery with polymer waterflooding in micromodels can recover as much oil as the two-stage process where the polymer waterflooding is preceded by waterflooding.

For each experiment, the micromodel was initially fully saturated with oil at a flow rate of 100 ml/h. After that, the oil was displaced by injecting dyed (5 w/w%, Ecoline®100, Royal Talens, The Netherlands) xanthan solution at a constant flow rate, using a syringe pump (PHD Ultra 3000, Harvard Apparatus), until steady state conditions were obtained.

Table 1
Carreau model [47] parameters and δ values for the shear rate – viscosity relations shown in Fig. 2.

C_p (ppm)	μ_0 (Pa s)	μ_∞ (Pa s)	λ (s)	n	δ
500	1.39×10^{-2}	1.79×10^{-3}	9.99×10^{-2}	4.65×10^{-2}	6.65×10^{-12}
1000	1.31×10^{-1}	1.98×10^{-3}	7.55×10^{-1}	4.16×10^{-2}	0.00728
2000	1.29	3.72×10^{-3}	3.24	3.05×10^{-2}	0

Table 2
Overview of flow rates and associated Darcy velocities for an experimental set, each conducted with 0, 500, 1000, and 2000 ppm dissolved xanthan gum injection solutions and repeated five times.

Experiment index i	Flow rate, Q_i (ml/h)	Darcy velocity, q_i (m/s)
1	10^{-2}	1.368×10^{-5}
2	10^{-1}	1.368×10^{-4}
3	10^{0}	1.368×10^{-3}
4	10^{1}	1.368×10^{-2}
5	10^{2}	1.368×10^{-1}

Steady-state pressure drops ΔP_i over the micromodel during monophasic flow of xanthan gum solutions were measured using a microfluidic pressure sensor (Elveflow, France) with a working range of 0–7 bars at q_1–q_4 for all values of C_p and at q_5 for C_p = 0 ppm and C_p = 500 ppm. For the two larger concentrations at q_5, the pressure drops were larger than the sensor could measure. The obtained (q_i, ΔP_i) data pairs for C_p = 0 were used to calculate the network permeability (k). The expression in Eq. (4), derived from the micromodel-specific Darcy equation, was used to compute the apparent viscosity (μ_{app}):

$$\mu_{app} = \frac{k}{q_i}\frac{\Delta P_i}{L} \tag{4}$$

The effluent fluid was sampled during injection of 2000 ppm xanthan solution at the highest flow rate. The rheogram of this effluent fluid (results not shown) was very close to that of the injected polymer, demonstrating that mechanical degradation during transport through the pore-network was not significant. In addition, no considerable plugging due to the polymer macromolecules was observed during these experiments.

A cleaning procedure prior to each experiment set was completed to restore the original condition of the medium. This procedure consisted of five consecutive rinses in the following order: deionized water, isopropanol, deionized water, SC-1 and deionized water. SC-1 stands for the first step of a Standard Clean [48] and was carried out at ~80 °C with a solution of 5 parts of deionized water, 1 part of aqueous NH_4OH (29 wt% NH_3) and 1 part of aqueous H_2O_2 (30 wt%). More than 100 pore volumes were injected at 100 ml/h during each rinse. After this cleaning step, the micromodel was dried by injecting pressurized air (1500 mbar) using a pressure generator (Elveflow, France). In addition, after each experiment, the micromodel was cleaned by completing three consecutives rinses with deionised water, isopropanol and deionised water, respectively, and then dried by injecting pressurized air.

2.4. Imaging and analysis

The dynamics and patterns of the interface displacement as well as the size distribution of the trapped oil ganglia were visualised using an optical microscope (Leica M205C, 20.5:1 zoom, 0.952 μm resolution, equipped with a Leica DFC 3000G high-resolution digital camera). Images were obtained before xanthan injection and after steady-state conditions were reached. Steady state was considered to have been reached once no significant fluid saturation changes were observed in the captured images. In these experiments, steady state was rapidly attained after xanthan breakthrough. In addition, complementary images were captured during displacement before breakthrough at flow rates Q_1 and Q_3 to investigate the patterns and morphology of the advancing front and the general dynamics of the displacement. The temporal resolution was 240 and 2 s for Q_1 and Q_3, respectively.

To delineate the patterns and morphology of the trapped phase as well as the flow regime, the obtained grey-scale images were analyzed using ImageJ software. The procedure followed for image analysis is quite similar to what was used in previously published work [9] described briefly in the following. To minimise the wall effects on the reported analysis, a square window with the size of 3.92 mm × 3.92 mm in the centre of the micromodel was considered for the image analysis. Additional evaluation was performed by changing the position and size of this window to ensure that the results in terms of residual oil saturation and blob size are representative of the whole porous medium. As for the image analysis, the reference image, representing oil-saturated micromodel at the onset of each test, was subtracted from the steady-state image in order to obtain an image displaying only the polymer solution phase, referred to as a "p-image". The p-image was then equalized to enhance its contrast, and two median filters (with the filtering radii of 2 and 3 pixels) were subsequently applied. After that, the filtered p-image was segmented using a variation of Yen Algorithm [49,50], giving the regions of the pore space filled with polymer solution at the steady state. The residual oil saturation (S_{ro}) was then calculated as the percentage of the pore space which was not filled with polymer solution. Additionally, the filtered p-images were segmented using a variation of the IsoData algorithm [51] to obtain the size distribution of the trapped ganglia. Then, the oil phase distribution was deduced as being the complementary part of the pore space. A median filter with a filtering radius = 2 was also applied to the oil phase and the average ganglia size and the ganglia size distribution were computed from the resulting images.

3. Results and discussions

3.1. Apparent and effective viscosity relations

Fig. 2(a) shows the measured pressure drop as a function of q. The pressure drops were then used to compute the apparent viscosity (μ_{app}) values with Eq. (4) and the results are shown in Fig. 2(b). The use of Eq. (4) is acceptable because no permeability reduction due to polymer retention was observed in our experiments. Indeed, xanthan gum macromolecules are flattened onto the surface so that the hydrodynamic thickness of the adsorbed layer is negligible [52]. Furthermore, the μ_{app} values obtained for monophasic flow of xanthan were considered to have essentially the same value for the immiscible displacement due to the low values of S_{ro} obtained (see Section 3.4). The results in Fig. 2b clearly show the shear-thinning behaviour of the xanthan solutions as the apparent viscosity decreases with increasing q.

We compared the apparent viscosity μ_{app} (Fig. 2b) with the effective viscosity μ (measured using the rheometer (Fig. 1b) to assess the effect of fluid-solid interactions on the fluid viscosity. To do so, we define the apparent shear rate $\dot{\gamma}_{app}$ in a porous medium as [52–54]:

$$\dot{\gamma}_{app} = \beta\frac{q}{\sqrt{k\varepsilon}} \tag{5}$$

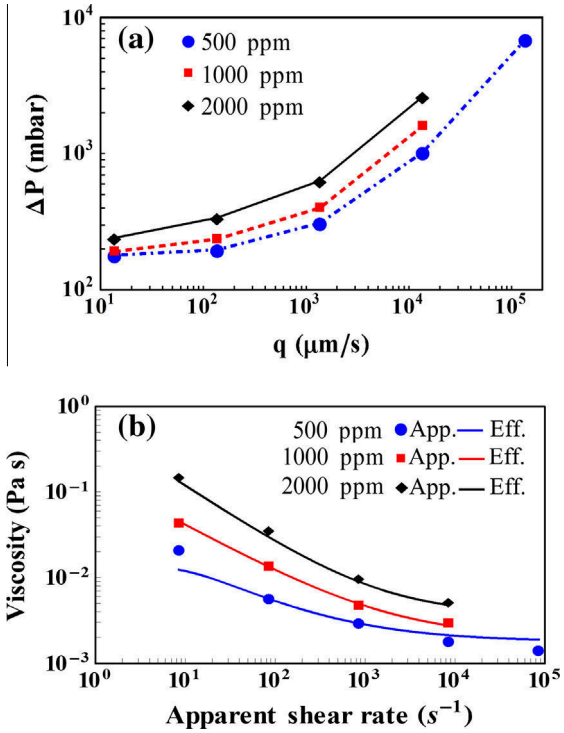

Fig. 2. (a) Pressure drop vs. q. (b) Apparent (symbols) and effective viscosity (solid lines) as a function of the shear rate for the 500, 1000, and 2000 ppm xanthan solutions.

where β is an empirical shift parameter which depends on the effective rheology and the pore structure. It has been reported that in spite of the diverse nature of the phenomena modifying rheology in porous media, the form of $\mu(\dot{\gamma})$ obtained using a rheometer is quite similar to that of $\mu_{app}(\frac{q}{\sqrt{kc}})$, except from the shift parameter β in the case of some polymer solutions such as xanthan gum aqueous solutions [53]. Fig. 2(b) shows the computed μ_{app} as a function of $\dot{\gamma}_{app}$ (symbols) and the effective viscosity relation fitted to the rheometer data. Assuming $\beta = 1$ a good correspondence between apparent and effective viscosities was obtained. In the case of C_p = 500 ppm, the difference between apparent and effective viscosity are more visible. This may arise from the fact that the order of magnitude of viscosity is smaller for C_p = 500 ppm (data are presented in logarithmic scale in Fig. 2) compared to the other concentrations, so eventual inaccuracies when approaching the limit of working range of the pressure sensor (0–7 bar) has a stronger impact on the apparent viscosity. This result means that the value of apparent viscosity at a given q in the used microfluidic device can be predicted from the effective viscosity as measured using the rheometer. Also, it shows that the effect of fluid-solid interactions (e.g. polymer mechanical degradation and apparent wall slip) on the relationship between viscosity and shear rate is negligible. Therefore, the same shear-thinning behaviour observed in the rheometer is reproduced during flow through the porous medium. Other researchers [30,31,33] found a good match between simulations and column and flow cell experiments by using $\beta = 2.4$. The good fit to experimental data provided by $\beta = 1$ in the present case may be due to the lesser viscosity reduction in micromodels as the apparent slip effects are expected to be negligible.

3.2. Polymer concentration effects on flow patterns

The capillary numbers and viscosity ratios corresponding to each polymer concentration at different flow rates are shown in Fig. 3. It should be noted that Ca and M values at the highest Darcy velocity (q_5) were only calculated for C_p = 0 ppm and C_p = 500 ppm because the high pressure drops generated at the two highest concentrations were out of the measurable range of our pressure sensor. Also, it is worthwhile to mention that the relation between Ca and M is linear for a constant q, which follows directly from the Ca and M definitions.

Fig. 3 shows that the value of Ca increases for a constant q as C_p increases. For example, the Ca corresponding at q_1 for C_p = 2000 ppm ($Ca = 6.31 \times 10^{-5}$) is two orders of magnitude larger than for C_p = 0 ppm ($Ca = 5.55 \times 10^{-7}$). When Ca increases (as a result of increasing C_p), viscous forces dominate the interface displacement. Therefore, capillary fingering will be less significant as C_p increases. However, this dominance of viscous forces at high C_p does not necessarily entail generation of large blobs by viscous fingering. Indeed, the viscous pressure drop of the injected fluid through the porous medium is higher at high C_p, which increases the mobilisation and fragmentation of oil ganglia, thus preventing the formation of large blobs. Moreover, Fig. 3 shows that the resulting range of Ca is narrower at higher C_p.

Furthermore, according to Fig. 3, the value of M increases as C_p increases for a constant q (meaning μ_{app} increases as C_p increases at a given value of q which is consistent with the results presented in Fig. 2(b)). In particular, this increase in M is more important at lower range of Ca as presented in Fig. 3. This is not a trivial conclusion, as it means that adding polymer to increase M is more effective at lower range of Ca or smaller q. In fact, the impact of C_p on M is relatively minor at high q as shown in Fig. 3. This is due to the orientation of xanthan macromolecules in the direction of flow, which leads to a reduced viscosity [53]. Therefore, the invasion front at high injection flow rates may not be stabilised by using polymer solutions. However, mobilisation and fragmentation of large ganglia may be still be enhanced by increasing C_p due to the higher viscous pressure drops of the invading fluid along the ganglia.

3.3. Interface displacement

The dynamics of the interface displacement as a function of C_p are shown in Fig. 4 for q_1 and q_3. In this figure, fluid saturations at times t, $t + \Delta t$, $t + 2\Delta t$ and $t + 3\Delta t$ are presented, with Δt being 240 s for q_1 and 2 s for q_3. t corresponds to the time at which the first image showing the invasion front is captured in each case, with the given temporal resolutions. Note that although the images are presented at the same flow rates, the corresponding capillary numbers are not the same (see Fig. 3). This Fig. shows that the invading front is stable at q_1 for all values of C_p. Indeed, no capillary fingering is observed even at q_1 and C_p = 0 ppm, and Ca is low

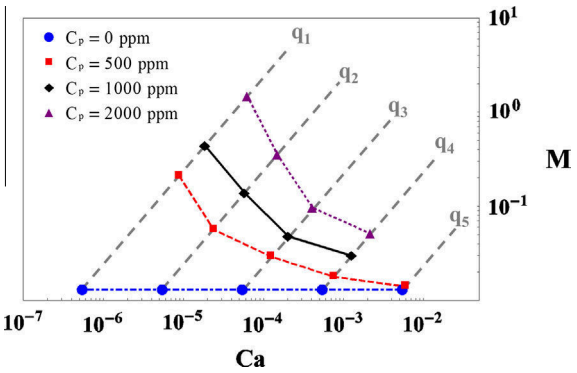

Fig. 3. Mobility ratio (M) as a function of the capillary number (Ca) for each C_p value.

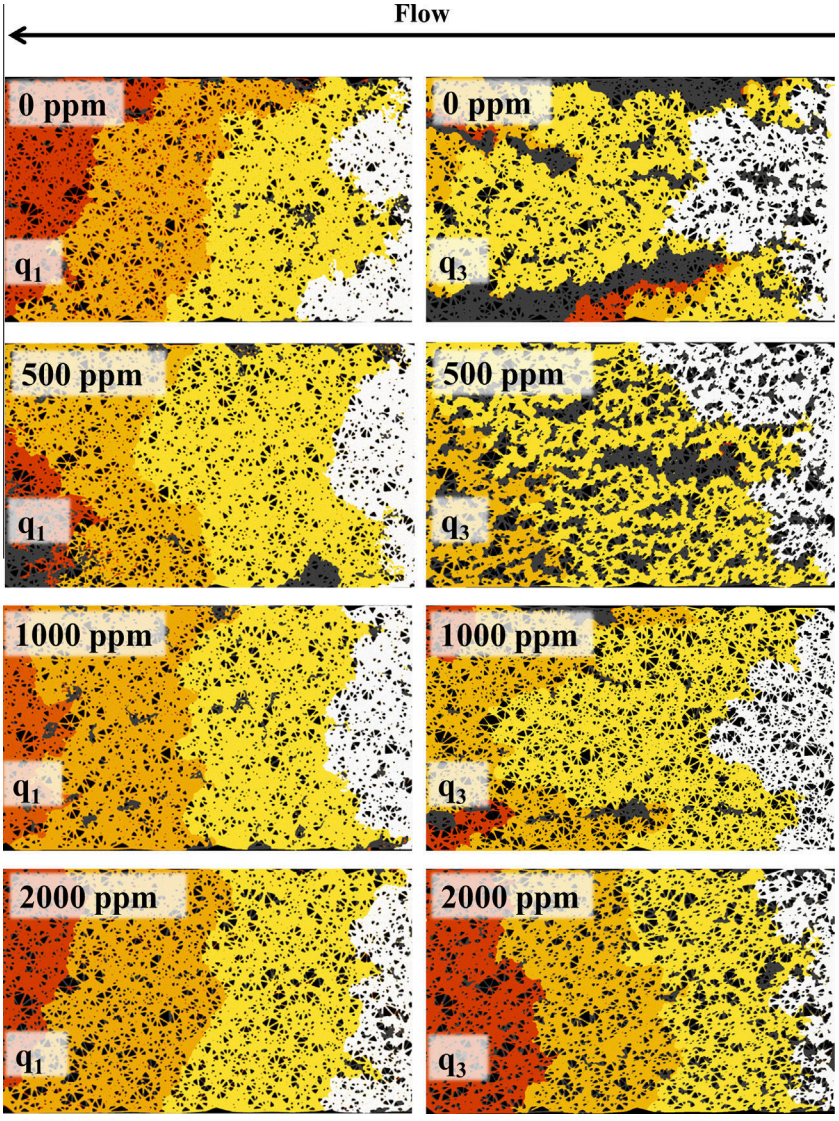

Fig. 4. Temporal evolution of fluid saturation for q_1 and q_3. The dark zones represent solid matter. White, light orange, dark orange and brown represent additional polymer solution saturations at times t, t + Δt, t + 2Δt and t + 3Δt respectively. Grey represents the regions of the pore space filled by oil at t + 3Δt.

enough so that viscous fingering is not important. Moreover, at the same low flow rate, the increase in Ca resulting from an increase in C_p is compensated by the simultaneous increase in M, ensuring the stability of the invading front. As a consequence, the number and size of ganglia trapped behind the front is small which leads to high oil recovery for all C_p. In contrast, viscous fingering leading to a large amount of bypassed oil is observed at q_3 and C_p = 0 ppm. At this higher flow rate, the increase of M with increasing C_p is more moderate than that for the displacement with q_1 (Fig. 3). However, the corresponding increase in Ca is also more moderate, leading to the front being progressively stabilised as C_p increases (Fig. 4). Moreover, it is worthwhile to mention that more but shorter fingers are formed at C_p = 500 ppm compared to waterflooding (C_p = 0 ppm). It should be noted that although the values of Ca corresponding to the experiment with C_p = 0 ppm at q_3 and C_p = 2000 ppm at q_1 are similar (Fig. 3), the displacement patterns and the amount of trapped oil are significantly different.

3.4. Efficiency of polymer waterflooding

Fig. 5(a) displays the average area of the trapped ganglia, computed using the segmented images, as a function of Ca. Results show that the average ganglia size at any Ca is effectively reduced by adding polymer to the injecting water. Indeed, the lowest average ganglia size was always obtained by the highest polymer concentration used in our experiments (2000 ppm). Also, it should be noted that within the q range imposed in our experiments, the variation in the ganglia size is lower at higher C_p. This may be, in part, a consequence of the narrower range of Ca covered for the same range of q at high C_p as mentioned in Section 3.2. Moreover, the maximum average ganglia size is lower at higher C_p. Fig. 5a shows that the largest blob sizes are obtained at intermediate values of Ca due to viscous fingering, dominating the propagation of the invading front, although M is unfavourable. It is also in this region that adding polymer to water is most effective in reducing the average ganglia size.

Residual oil saturations (S_{ro}) were calculated from the segmented images and represented as a function of q in Fig. 5(b) showing that S_{ro} reduces in the case of polymer waterflooding compared to waterflooding for all q values. This is in good agreement with the work of other researchers [2], who presented the steady-state phase distribution during oil displacement by a shear-thinning fluid. Our results show that the recovery efficiency is improved at all polymer concentrations compared to

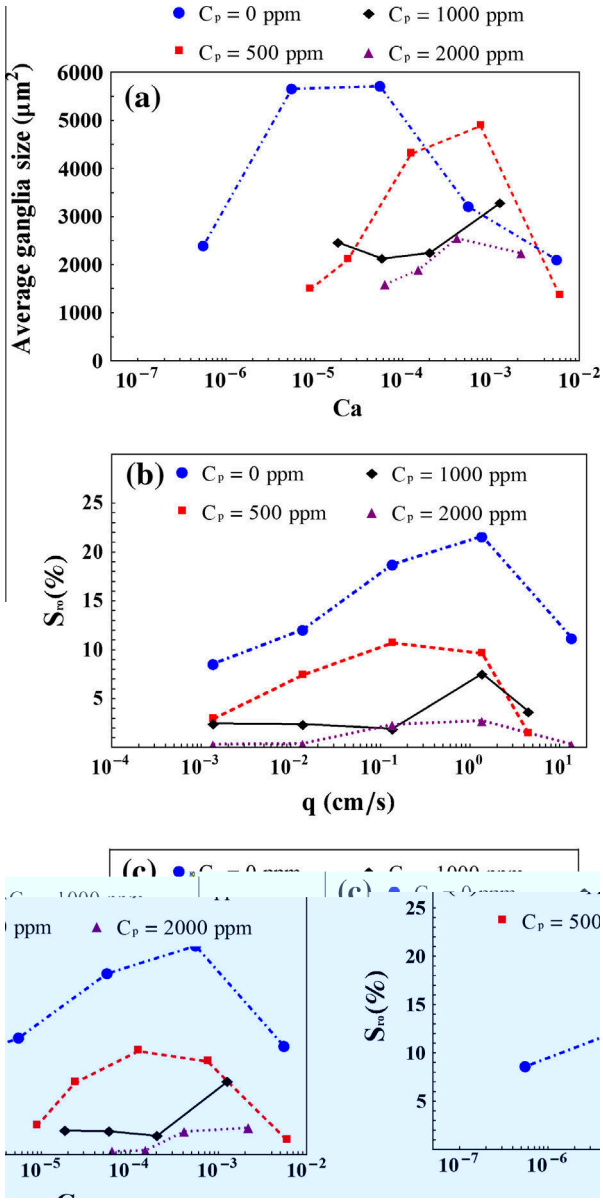

Fig. 5. (a) Average ganglia size as a function of Ca. (b) S_{ro} as a function of q, (c) S_{ro} as a function of Ca.

waterflooding and that the general trend of S_{ro} is to decrease as C_p increases. Indeed, the lowest S_{ro} values are obtained at the highest C_p for all q. One can relate the decrease of S_{ro} to the stabilisation of the invasion front induced by the higher viscosity ratios as C_p is increased. However, it should be noted that not only does M increase with C_p for a given flow rate, but also Ca (as shown in Fig. 3), which may in turn favour destabilisation of the front leading to higher S_{ro}. Therefore, in order to avoid misinterpretation of the results and to make an analogy with CDCs commonly used in the case of Newtonian fluids, S_{ro} is also represented as a function of Ca in Fig. 5c.

Fig. 5c shows that S_{ro} decreases with increasing C_p at every value of overlapping Ca values considered in our study. A possible interpretation is that the front-stabilising effect as a result of higher M (due to the higher polymer concentrations) overcomes the front-destabilising effect due to the increase in Ca, leading to less oil being trapped behind the front. Moreover, it should be noted that high viscosities of the concentrated polymer solutions generate high viscous pressure drops that are capable of mobilising or fragmenting the large ganglia easier than diluted polymer solutions. In addition, Fig. 5(c) shows that the effect of Ca on S_{ro} is less pronounced at higher C_p. It should be noted that in the case of C_p = 1000 ppm, average ganglia size increases at the lowest value of Ca, and S_{ro} slightly decreases at intermediate values of q, which is not the case for the other concentrations. This behaviour has been reported before [9,56,57], and requires further investigation. The results presented in Fig. 5 show that S_{ro}(Ca) curves (CDCs) are non-monotonic at every C_p, which is in agreement with recent findings [9,55].

The crossover between three regimes of fluid displacements, capillary-controlled displacement (capillary fingering), unstable viscous displacements (viscous fingering) and stable or compact viscous displacements, was investigated by several researchers [9,12–14] and results were typically presented in a M-Ca phase diagram. To map our results based on phase behaviour we present residual saturation of the experiments based on Ca and M in the three-dimensional plot shown in Fig. 6. One can observe that S_{ro} monotonically decreases with increasing M, attaining a plateau of very low S_{ro} above a critical value of roughly Log M > −1.5. Furthermore, once M is greater than this critical value and because Ca has limited influence on S_{ro}, a stable region with low S_{ro} values is observed. The reason is that in two-phase immiscible displacement with shear-thinning polymer solutions, the highest M are obtained at low values of Ca (see Fig. 3) when polymer molecules are not aligned in the direction of flow. This results in a "*double stabilising effect*" which impedes viscous fingering.

3.5. Ganglia size distribution and analysis

Ganglia size distributions were computed from the segmented images corresponding to the four values of C_p and three selected values of q (q_1, q_3, q_5) as presented in Fig. 7. q was chosen instead of Ca because the values of Ca are different for each C_p whereas the values of q are identical, which facilitates comparison. Fig. 7 shows that in the case of C_p = 0 ppm and C_p = 500 ppm, the ganglia size increases from q_1 to q_3, but decreases from q_3 to q_5. This may stem from the fact that, at highly unfavourable viscosity ratios (low C_p), viscous fingering becomes important at intermediate values of q leading to generation of larger ganglia. These large ganglia are fragmented or mobilised at high values of q, resulting in smaller trapped blobs. This confirms earlier numerical predictions [12,57]. In contrast for C_p = 1000 ppm the range of ganglia sizes remain similar at q_1 and q_3 before decreasing at q_5. Ganglia sizes are roughly independent of q for C_p = 2000 ppm, which may arise

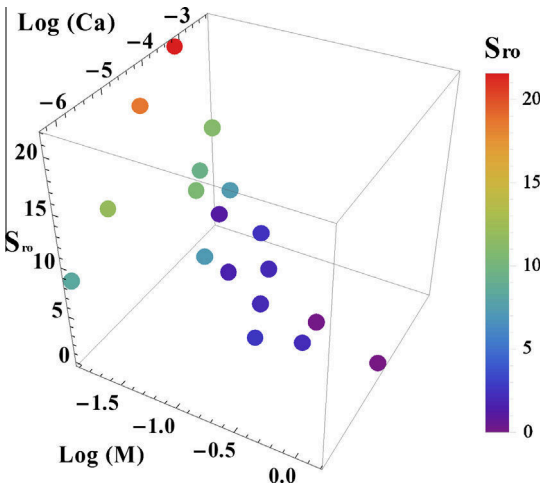

Fig. 6. Three-dimensional plot showing S_{ro}(%) as influenced by Ca and M.

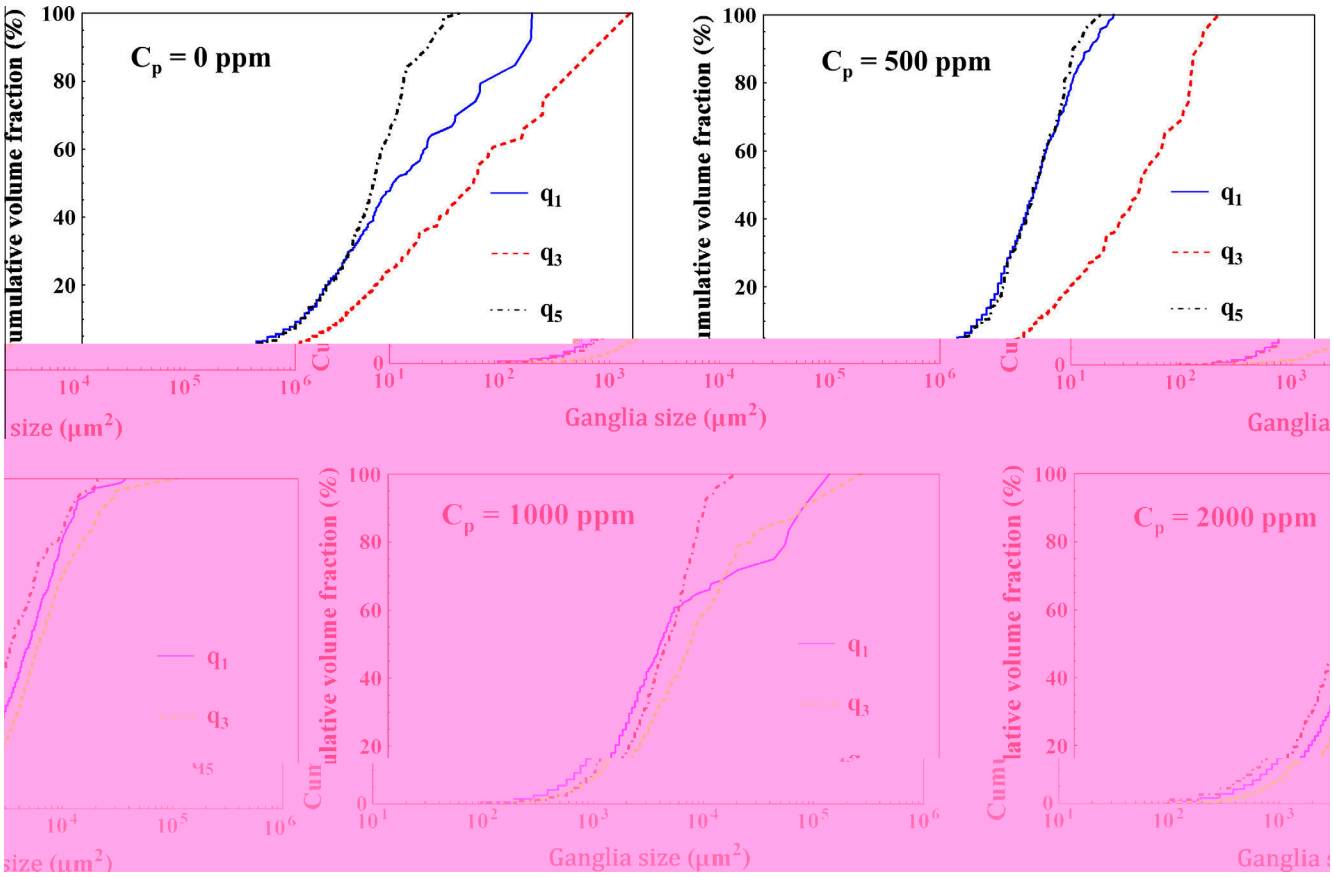

Fig. 7. Cumulative ganglia size distribution for all xanthan solutions injected with q_1, q_3, and q_5.

from generation of more stable invading fronts as a consequence of the higher values of M. Closer inspection of Fig. 7 reveals that most ganglia sizes generated when viscous fingering is not important are comprised in the range ~10^2 to 10^4 μm², whereas the size distributions are wider when viscous fingering occurs. Also, it may be noted that the differences between size distributions at different q are less important as C_p increases.

According to the percolation theory, the size distribution of the trapped nonwetting phase in a porous medium after imbibition at infinitesimally low flow rates should scale as a power-law expressed as [8,58–60]:

$$N(s) \sim s^{-\tau} \tag{6}$$

where s is the number of the pores saturated by a trapped nonwetting ganglia, N is the number of ganglia whose size equals to s pores, and τ is the power-law exponent. Values of τ slightly <2 were obtained using numerical simulations in two-dimensional structures [59]. Using the images obtained in our experiments, we investigated the potential presence of such a power-law in our system in the case of the two lowest Darcy velocities (q_1 and q_2). The analysis was refined by only taking into account the ganglia sizes larger than 10 pixels, occurring more than once. It is noted that this scaling approach should be applied to the size of the ganglia in number of pores instead of their surface in pixels. However, given that the pore size distribution of our micromodel was relatively narrow and the depth of the channels was constant, both approaches are approximately equivalent. Other authors [8] followed a similar approach with three-dimensional images obtained by microtomography. We defined the normalized count as (number of ganglia with a given surface in pixels)/(number of smallest ganglia) and the normalized size as (surface)/(surface of the smallest ganglia). The normalized count was represented as a function of the normalized size in all cases, and the corresponding power-law relations are shown in the electronic supporting materials section of this article, together with the best-fit τ values.

The average of τ values presented in Fig. 8 is 1.90, which is in agreement with the numerical predictions of 1.8–1.84 previously presented in the literature for two-dimensional networks based on the invasion percolation theory [59]. Also, in spite of the variations in Ca induced by the different C_p and q considered here, the obtained exponents are quite close as illustrated in Fig. 8. It must be mentioned that the exact value of τ is influenced by how the curve fitting is performed and the range of ganglia sizes used for fitting the power law.

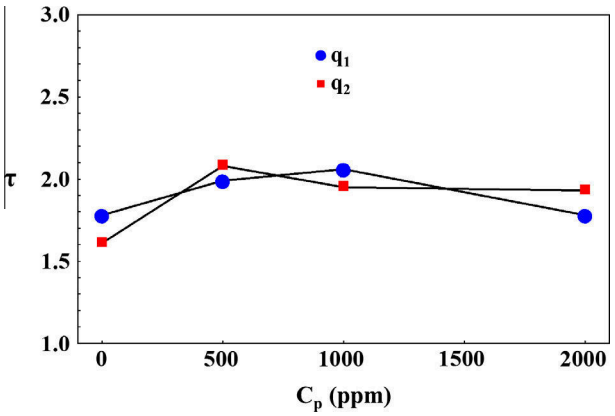

Fig. 8. Fitted power-law τ values as a function of the polymer concentration C_p at the lowest Darcy velocities, q_1 and q_2 applied in our experiments.

4. Summary and conclusions

Understanding the interfacial processes involved in multiphase flow of shear-thinning fluids in porous media at the pore scale is of vital importance in EOR, soil remediation, and other environmental and engineering applications. These fluids are characterized by the dependency of their apparent viscosity on the injection flow rate, leading to different values of M at different flow rates. For this reason, the Newtonian assumption used in the common approaches for the analysis of immiscible displacement in porous media and phase entrapment [9,12–14], e.g., stability diagrams, CDCs and ganglia size distributions as a function of Ca, do not apply when a shear-thinning fluid is used as the invading fluid. Moreover, flooding experiments with shear-thinning polymer solutions previously presented in the literature [20,27] have only analyzed the effect of polymer concentration on front stabilization and recovery efficiency at a single flow rate without evaluating the influence of Ca.

Previous works reported the need of studying the effects of polymer concentration on the oil recovery performance using laboratory experiments [61]. In particular, CDCs are essential inputs in typical reservoir simulation software for EOR [9,21]. In response to this need, we have now demonstrated that the polymer concentration C_p has a significant influence on the dynamics and patterns of interface displacement and phase distribution (even when the flowrate is kept constant) due to the effects of C_p on the effective viscosity of the polymer solution. In contrast to previous studies [2,20,24–28], the dependency of M and S_{ro} on Ca could be analyzed. Using a series of microfluidic experiments, we showed the capability of C_p to alter the value and range of Ca and M, which, in turn, determine the stability of the invasion front as well as the mobilisation and fragmentation of the resulting ganglia. We found that the effect of fluid-solid interactions on the relationship between viscosity and shear rate is negligible in the conducted microfluidic experiments, in agreement with the experiments by Chauveteau [52]. It was also shown that adding polymer, thus increasing Ca and M, is more effective at a lower flow rate.

In our experiments, polymer waterflooding proved to be more efficient to displace oil than waterflooding, confirming previous results [2], regardless of the value of C_p. Moreover, S_{ro} decreased with increasing C_p at all tested Ca values and the CDCs were found to be non-monotonic at every C_p, extending the results recently published for packs of glass beads and micromodels [9,55] to the case of polymer waterflooding. This suggests that it may be possible to attain similar oil recoveries both in polymer and regular waterfloods under injection flow rates which differ by several orders of magnitude. The highest M is obtained at low values of Ca when polymer molecules are not aligned in the direction of flow, resulting in a "*double stabilizing effect*" of the displacing interface which impedes viscous fingering. We found that the dependency of S_{ro} and the ganglia sizes on the flow rate is less pronounced at high values of C_p. In particular, S_{ro} was found to be independent of Ca above a critical value of M. Using a percolation theory approach, we obtained that the average power-law exponent in our experiments was in agreement with the numerical predictions previously presented for 2D networks [59]. Moreover, the values of the power-law exponents obtained at low flow rates were found to be close for all the values of C_p considered in our work.

This micromodel study enabled us to maximize our control over the boundary conditions and focus on the effects of C_p on Ca, M and the residual oil saturation. This work indicates a starting point towards the development of quantitative tools for the analysis of oil recovery efficiency using shear-thinning fluid. The presented results should now be extended to more complex 3D geometries in future work. Also, the obtained relationships can be implemented in reservoir simulation software for EOR in order to provide a more realistic alternative to the Newtonian assumption, which is expected to result in a better estimation of recovery efficiency at the pilot plant and reservoir scales. In particular, these results may provide useful guidance on the selection of the injection flow rate when using shear-thinning fluids in the mentioned applications.

Acknowledgments

Nima Shokri would like to acknowledge the donors of the American Chemical Society Petroleum Research Fund for support of this research (PRF No. 52054-DNI6) and the equipment funding from The Royal Society (RG140088). We thank Nikolaos Karadimitriou who designed the micromodel. The micromodel was fabricated in the William R. Wiley Environmental Molecular Sciences Laboratory, a U.S. Department of Energy scientific user facility operated by Pacific Northwest National Laboratory.

Appendix A. Supplementary material

Supplementary data associated with this article can be found, in the online version, at http://dx.doi.org/10.1016/j.jcis.2016.03.027.

References

[1] M. Sahimi, Flow and Transport in Porous Media and Fractured Rock: From Classical Methods to Modern Approaches, Wiley-VCH Publishers, Weinheim, Germany, 2011. 733 pp.
[2] M.A. Nilsson, R. Kulkarni, L. Gerberich, R. Hammond, R. Singh, E. Baumhoff, J.P. Rothstein, J. Nonnewton. Fluid Mech. 202 (2013) 112–119.
[3] P. Grassia, E. Mas-Hernandez, N. Shokri, S.J. Cox, G. Mishuris, W.R. Rossen, J. Fluid Mech. 751 (2014) 346–405.
[4] M. Hashemi, B. Dabir, M. Sahimi, AIChE J. 45 (1999) 1365–1382.
[5] Y.C. Yortsos, D. Salin, J. Fluid Mech. 557 (2006) 225–236.
[6] B. Raeesi, M. Piri, J. Hydrol. 376 (2009) 337–352.
[7] V. Joekar-Niasar, S.M. Hassanizadeh, L.J. Pyrak-Nolte, C. Berentsen, Water Resour. Res. 45 (2010) W02430.
[8] T. Pak, I.B. Butler, S. Geiger, M.I.J. van Dijke, K.S. Sorbie, PNAS 112 (2015) 1947–1952.
[9] A. Rodríguez de Castro, N. Shokri, N. Karadimitriou, M. Oostrom, V. Joekar-Niasar, Water Resour. Res. 51 (2015) 8517–8528, http://dx.doi.org/10.1002/2015WR017727.
[10] D. Wilkinson, Phys. Rev. A 30 (1984) 520–531.
[11] N. Shokri, P. Lehmann, P. Vontobel, D. Or, Water Resour. Res. 44 (2008) W06418, http://dx.doi.org/10.1029/2007WR006385.
[12] M.M. Dias, A.C. Payatakes, J. Fluid Mech. 164 (1986) 305–336.
[13] R. Lenormand, E. Touboul, C.J. Zarcone, Fluid Mech. 189 (1988) 165–187.
[14] M. Sahimi, Rev. Mod. Phys. 65 (4) (1993) 1393–1534.
[15] Y. Méheust, G. Løvoll, K.J. Måløy, J. Schmittbuhl, Phys. Rev. E 66 (2002) 051603–51612.
[16] D. Or, Adv. Water Resour. 31 (2008) 1129–1136.
[17] L.P. Dake, Fundamentals of Reservoir Engineering, Elsevier, 1978. 462 pp.
[18] D. Wilkinson, Multiphase flow in porous media, in: N. Boccara, M. Daoud (Eds.), Physics of Finely Divided Matter, Springer, 1985, pp. 280–288.
[19] P. Meakin, J.M. Deutch, J. Chem. Phys. 85 (1986) 2320–2325.
[20] M. Buchgraber, T. Clemens, L.M. Castanier, A.R. Kovscek, SPE Reservoir Eval. Eng. 14 (2011) 269–280.
[21] R. Oughanem, S. Youssef, B. Bazin, E. Maire, O. Vizika, Pore-scale to core-scale aspects of capillary desaturation curves using CT-scan imaging, in: Proceedings of the 17th European Symposium on Improved Oil Recovery, Saint Petersburg, 2013.
[22] E.C. Donaldson, G.V. Chilingarian, T.F. Yen, Enhanced Oil Recovery II: Processes and Operations, Elsevier, Amsterdam, 1989.
[23] J.J. Sheng, Modern Chemical Enhanced Oil Recovery, Theory and Practice, GPG, Elsevier, 2011.
[24] W.B. Gogarty, SPE 1566, SPE J. 7 (2) (1967) 161–173.
[25] J.L. White, H.M. Phillips, J.E. Goddard, B.D. Baker, SPE 3672 J. Pet. Technol. 25 (2) (1973) 143–150.
[26] D.W. Green, G.P. Willhite, Enhanced Oil Recovery, second ed., Textbook Series, vol. 6, Society of Petroleum Engineers, Richardson, 2003.
[27] H.E. Meybodi, R. Kharrat, X. Wang, Transp. Porous Media 89 (1) (2011) 97–120.
[28] T. Clemens, K. Tsikouris, M. Buchgraber, L. Castanier, A. Kovscek, Soc. Pet. Eng. 16 (2013) 144–154, http://dx.doi.org/10.2118/154169-MS.

[29] L. Zhong, M. Oostrom, M.J. Truex, V.R. Vermeul, J. Szecsody, J. Hazard. Mater. 244–245 (2013) 160–170.
[30] C. Chokejaroenrat, N. Kananizadeh, C. Sakulthaew, S. Comfort, Y. Li, Environ. Sci Technol. 47 (2013) 13031–13038.
[31] K.E. Martel, R. Martel, R.J. Lefebvre, P.J. Gelinas, Groundw. Monit. Remediat. 18 (1998) 103–113.
[32] J.A.K. Silva, M. Smith, J. Munakata-Marr, J.E. McCray, J. Contam. Hydrol. 136 (2012) 117–130.
[33] L. Zhong, M. Oostrom, T.W. Wietsma, M.A. Covert, J. Contam. Hydrol. 101 (2008) 29–41.
[34] M. Truex, V.R. Vermeul, D.T. Adamson, M. Oostrom, L. Zhong, R.D. Mackley, B.G. Fritz, J.A. Horner, T.C. Johnson, J.N. Thomle, D.R. Newcomer, C.D. Johnson, M. Rysz, T.W. Wietsma, C.J. Newell, Groundw. Monitor. Remediat. 35 (2015) 34–45, http://dx.doi.org/10.1111/gwmr.12101.
[35] S.W. Chapman, B.L. Parker, Water Resour. Res. 41 (2005) W12411.
[36] T. Willingham, C. Zhang, C.J. Werth, A.J. Valocchi, M. Oostrom, T.W. Wietsma, Adv. Water Res. 33 (2010) 525–535.
[37] J.W. Grate, M.G. Warner, J.W. Pittman, K.J. Dehoff, T.W. Wietsma, C. Zhang, M. Oostrom, Water Resour. Res. 49 (2013) 4724–4729.
[38] N.K. Karadimitriou, M. Musterd, P.J. Kleingeld, M.T. Kreutzer, S.M. Hassanizadeh, V. Joekar-Niasar, Water Resour. Res. 49 (2013) 2056–2067.
[39] F. Garcia-Ochoa, V.E. Santosa, J.A. Casasb, E. Gómez, Biotechnol. Adv. 18 (2000) 549–579.
[40] A.Z. Abidin, T. Puspasari, W.A. Nugroha, Proc. Chem. 4 (2012) 11–16.
[41] A. Palaniraj, V. Jayaraman, J. Food Eng. 106 (2011) 1–12.
[42] V.S. Wadhai, A.N. Dixit, Indian Streams Res. J. 1 (2011) 1–4.
[43] Y.-Q. Song, Cem. Concr. Res. 37 (2007) 325–328.
[44] A. Mongruel, M. Cloitre, J. Non-Newton Fluid Mech. 110 (2003) 27–43.
[45] A. Rodríguez de Castro, Flow Experiments of Yield Stress Fluids in Porous Media as a New Porosimetry Method PhD thesis, Arts et Métiers ParisTech, 2014.
[46] A. Rodríguez de Castro, A. Omari, A. Ahmadi-Sénichault, D. Bruneau, Transp. Porous Media 101 (3) (2014) 349–364.
[47] P.J. Carreau, Trans. Soc. Rheol. 16 (1972).
[48] W. Kern, J. Electrochem. Soc. 137 (1990) 1887–1892.
[49] J.C. Yen, F.J. Chang, S. Chang, IEEE Trans. Image Process. 4 (3) (1995) 370–378.
[50] M. Sezgin, B. Sankur, J. Electron. Imaging 13 (1) (2004) 146–165.
[51] T.-W. Ridler, S. Calvard, Man Cybernet. 8 (1978) 630–632.
[52] G. Chauveteau, J. Rheol. 26 (2) (1982) 111–142.
[53] K.S. Sorbie, Polymer-Improved Oil Recovery, Blackie and Son Ltd, 1991.
[54] X. López, P.H. Valvatne, M.J. Blunt, J. Colloid Interface Sci. 264 (2003) 256–265.
[55] H. Khosravian, V. Joekar-Niasar, N. Shokri, AIChE J. 61 (2015) 1385–1390.
[56] V.A. Tabrizy, J. Pet. Eng. 2014 (2014) 1–16, http://dx.doi.org/10.1155/2014/430309.
[57] M. Singh, K.K. Mohanty, Chem. Eng. Sci. 58 (2003) 1–18.
[58] D. Stauffer, Phys. Rep. 54 (1) (1979) 1–74.
[59] D. Wilkinson, J.F. Willemsen, J. Phys. A: Math. Gen. 16 (1983) 3365–3376.
[60] M. Sahimi, Heterogeneous Materials I: Linear Transport and Optical Properties, Springer-Verlag, New York, 2003. 691 pages.
[61] F. Douarche, D. Rousseau, B. Bazin, R. Tabary, P. Moreau, M. Morvan, Oil & Gas Sci. Technol. – Rev. IFP Energies Nouvelles 67 (2012) 983–997.